Energy relaxation in $(La_{0.6}Pr_{0.4})_{0.7}Ca_{0.3}MnO_3$ films across the metal-insulator transition

Cinja Seick,[1,*] Karen Stroh,[1,*] Tim Titze,[1] Vitaly Bruchmann-Bamberg,[1] Andreas Weisser,[1] Stefan Mathias,[1,2] Vasily Moshnyaga,[1] Henning Ulrichs,[1] and Daniel Steil[1,†]

[1]*I. Physikalisches Institut, Universität Göttingen, 37077 Göttingen, Germany*

[2]*International Center for Advanced Studies of Energy Conversion (ICASEC), Universität Göttingen, 37077 Göttingen, Germany*

(Received 17 February 2022; revised 3 November 2022; accepted 17 January 2023; published 9 February 2023)

The colossal magnetoresistive manganite $(La_{0.6}Pr_{0.4})_{0.7}Ca_{0.3}MnO_3$ (LPCMO) undergoes a ferromagnetic (FM) metal to paramagnetic insulator phase transition at around 195 K, which develops via an intermediate polaronic state strongly susceptible to external magnetic fields. Transient reflectivity studies of LPCMO on timescales from sub-picoseconds to nanoseconds reveal that the overall system dynamics are strongly influenced by the phase transition with a sharp and strong decrease in the relaxation time while crossing from the ferromagnetic metallic phase into the paramagnetic insulating phase. We show that the long relaxation times of the reflectivity after nonequilibrium excitation within the FM phase are caused by the slow recovery of the ordered FM state after laser-induced demagnetization. Control of the nonequilibrium dynamics close to the phase transition is demonstrated by applying moderate magnetic fields below 1 T.

DOI: 10.1103/PhysRevB.107.085115

I. INTRODUCTION

The long-term interest in perovskite manganites, like $RE_{1-x}A_xMnO_3$ (RE = La, Pr, Nd, etc. and A = Ca, Sr, etc.), is stimulated by the intriguing interplay of charge, spin, and lattice degrees of freedom, which results in rich phase diagrams [1] and enables an efficient control of properties by external fields [2] as well as by material design in thin films and heterostructures [3]. The so-called colossal magnetoresistance (CMR) effect [4–6], i.e., a magnetic-field-induced insulator-metal transition, has been observed in many thin manganite films, e.g., $La_{1-x}Ca_xMnO_3$ (LCMO) [7], $Pr_{1-x}Ca_xMnO_3$ (PCMO) [2], and $(La_{1-y}Pr_y)_{0.7}Ca_{0.3}MnO_3$ (LPCMO) [8]. According to the commonly accepted theoretical interpretation [9,10], CMR originates from a nanometer-scaled electronic phase separation in the vicinity of the first-order ferro-/paramagnetic phase transition (PT) with competing ferromagnetic metallic (FMM) order due to the double exchange interaction [11–13] and antiferromagnetic insulating order due to charge-ordering regions. Experiments on bandwidth-controlled LPCMO films [14] revealed that CMR is underlined by an intrinsic antiferromagnetic (AFM) coupling of the ferromagnetic (FM) domains mediated by correlated polarons, i.e., static short-range ordered Jahn-Teller (JT) distortions with the ordering wave vector $(\frac{1}{4}, \frac{1}{4}, 0)$ and coherence length of ∼1–2 nm as quantified in bulk manganites by previous neutron and x-ray studies [15–18]. A recent Raman spectroscopy study [19] evidenced that, similar to CMR, the concentration of correlated JT polarons depends drastically on temperature and magnetic field close to the PT. All these studies underscore the fundamental role of correlated JT polarons as mediators of strong electron-phonon coupling and actuators of the CMR mechanism.

Ultrafast optical spectroscopy allows one to study fundamental processes of energy transfer between quasiparticles (QPs) in correlated materials by accessing the nonequilibrium between electrons, spins, and the lattice. Probing the energy exchange and dissipation processes between different degrees of freedom allows one to investigate the changes in their couplings across phase transitions. We study temperature- and magnetic field-dependent energy relaxation dynamics in an LPCMO thin film across the first-order PT from sub-picoseconds to nanoseconds using pump-probe transient reflectivity with the aim to understand the roles of correlated polarons and ferromagnetic spin ordering for energy relaxation dynamics. To the best of our knowledge, there are no reports on the dynamics of photoexcited charge carriers in this context in LPCMO. Published works on dynamics in LPCMO have so far concentrated on sub-picosecond- to picosecond-timescale structural dynamics in LPCMO crystal and film samples with strongly different ferromagnetic and charge-ordering temperatures [20,21].

In the present paper, we compare the energy transfer processes after a femtosecond optical excitation in the (i) low-temperature FMM, (ii) intermediate polaronic insulating, and (iii) high-temperature paramagnetic insulating (PMI) states. Crossing the FM PT by temperature or magnetic field, we observe that a significant modification of the overall nonequilibrium reflectivity dynamics occurs in agreement with earlier reports on the related CMR-material LCMO [22–24]. From our experimental data in combination with finite-difference time-domain (FDTD) simulations, we conclude that the observed strong increase in the long-term relaxation time within the FM phase compared to the PM phase is caused by a slow recovery of the spin-ordered ground state after laser-

*These authors contributed equally to this work.
†dsteil@gwdg.de

induced spin disordering. Furthermore, we demonstrate that the observed nonequilibrium dynamics close to the PT can be strongly tuned not only by temperature but also by moderate magnetic fields $B < 1$ T, which is a direct consequence of the presence of the polaronic QPs. This tunability makes LPCMO a unique advanced functional material.

II. EXPERIMENTAL DETAILS

We investigate $(La_{1-y}Pr_y)_{1-x}Ca_xMnO_3$ with $x \approx 0.3$ and $y \approx 0.4$. This composition exhibits a coupled ferromagnetic-to-paramagnetic and metal-to-insulator (MI) phase transition with a Curie temperature $T_C \sim 200$ K [14,25]. The sample is a 56-nm-thick LPCMO film grown heteroepitaxially and strain-free [26,27] on an MgO(200) substrate using metalorganic aerosol deposition (MAD) [28,29]. Details on sample structure can be found in Ref. [14], where similar MAD-grown films have been investigated by, e.g., high-resolution transmission electron microscopy geometric phase analysis regarding strain, x-ray diffraction, atomic force microscopy, and Raman spectroscopy. The magnetic phase transition and CMR have been measured by temperature- and magnetic-field-dependent superconducting quantum interference device (SQUID) magnetometry and by four-probe electrical resistance using a physical property measurement system, respectively. According to the logarithmic derivative, the Curie and MI transition temperatures of the film are $T_C = 194$ K and $T_{MI} = 185$ K, respectively. The sample shows a pronounced CMR $= 100\%[R(0) - R(B)]/R(B) > 2000\%$ already for $B = 1$ T (see Fig. S1 in the Supplemental Material (SM) [30]). For static optical characterization, the transmission $\mathcal{T}$ and the reflection $\mathcal{R}$ of the LPCMO film were measured using unpolarized light in the ultraviolet (UV)-visible (200–1100 nm) and near infrared (NIR) (900–2100 nm) spectral ranges for temperatures $T = 40$–300 K using a liquid-helium continuous-flow cryostat. As a result, the absorption coefficient α [31,32] and the complex refractive index [33,34] (see SM [30] for more details) were determined, which serve as material parameters for FDTD simulations.

Transient changes of the reflectivity $\Delta\mathcal{R}(t)$ up to 1.1 ns timescale were measured using a bichromatic pump-probe setup utilizing a femtosecond fiber amplifier system operating at a repetition rate of 50 kHz. In this setup, the fundamental femtosecond light pulses with a central wavelength of 1030 nm (1.2 eV photon energy) and their second harmonic at a 515 nm central wavelength (2.4 eV photon energy) are used as pump and probe pulses, respectively. Both pulses have a duration of less than 40 fs at the sample position, which is close to the Fourier limit. Temperature control is realized by using a liquid-helium cryostat with optical access placed in between the poles of a variable-gap electromagnet allowing for external magnetic fields, $B = 0$–0.8 T. Details can be found in the SM [30].

III. EXPERIMENTAL RESULTS

A. Nonequilibrium dynamics at the picosecond to nanosecond timescale

Figure 1 shows an exemplary set of transient reflectivity (TR) data recorded at an incident optical fluence of $F = 5.9\,\mathrm{mJ/cm^2}$ for three characteristic temperatures: $T_1 = 175$ K $< T_C$, $T_2 = 195$ K $\approx T_C$, and $T_3 = 250$ K $> T_C$ for $B = 0$ (light colors) and for an applied magnetic field of $B = 0.8$ T (dark colors). Additional data for other temperatures are presented in the SM [30]. As evident from Fig. 1(a), at a timescale of $t \sim 0$–20 ps, all reflectivity curves $\Delta\mathcal{R}(t)$ show the following qualitatively similar features: (A) a very fast increase of $\Delta\mathcal{R}(t)$ due to laser excitation which corresponds to the fast thermalization of excited electrons by electron-electron and electron-phonon scattering and (B) a peaklike structure at $t \approx 9$ ps, which is related to Brillouin scattering in the film (see SM for details [30]). For longer timescales up to 1100 ps [Fig. 1(b)], the relaxation depends strongly on the electronic state of LPCMO. In the PMI state at $T = 250$ K (far away from T_C), $\Delta\mathcal{R}(t)$ decays exponentially (D) and relaxation does not depend on the applied magnetic field. In the FMM state, the reflectivity dynamics changes distinctly, acquiring a significantly growing part for times up to ~300 ps (C), followed by a decrease at larger times (D). Remarkably, close to the PT at $T = 195$ K, but still in the insulating state, a moderate applied magnetic field, $B = 0.8$ T, switches the relaxation behavior to the characteristic of the FMM state. This indicates a field-induced PMI/FMM phase transition in the electron dynamics and highlights a modification of the pathways for equilibration processes of internal energy at the PT. Such magnetic field-induced effects are still visible within the FMM state close to the PT at $T = 175$ K.

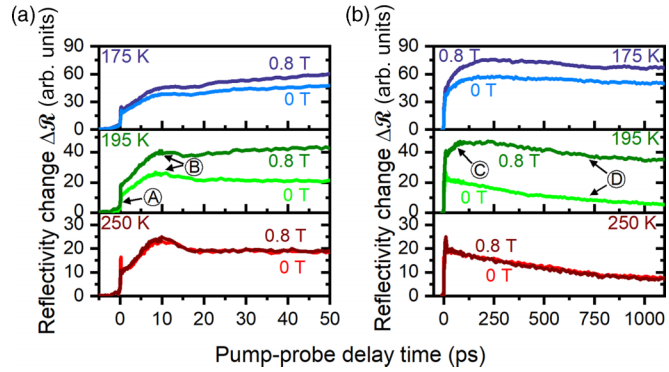

FIG. 1. Nonequilibrium dynamics in the LPCMO film after femtosecond-laser pulse excitation with an incident fluence of $F = 5.9\,\mathrm{mJ/cm^2}$. Three different temperatures have been selected from two warming cycles: 175 K $< T_C$ (blue curves), 195 K $\approx T_C$ (green curves), and 250 K $> T_C$ (red curves). Panel (a) shows a zoom into the first 50 ps after excitation, and panel (b) depicts reflectivity dynamics up to 1.1 ns. All panels contain data for zero field and for $B \approx 0.8$ T. Letters in circles refer to different processes discussed in the main text.

To analyze the transient reflectivity in more detail, the following phenomenological expression was fitted to the data:

$$\Delta\mathcal{R}(t) = B\exp\left(\frac{-(t-t_p)^2}{2\omega^2}\right) - \sum_{i=1}^{4} A_i \exp\left(\frac{-t}{\tau_i}\right), \quad (1)$$

where the Gaussian function models the signal maximum at $t_p \approx 9$ ps, and the superposition of exponential functions models the excitation and relaxation processes. Depending on the phase state of the system, two (PMI) or three (FMM)

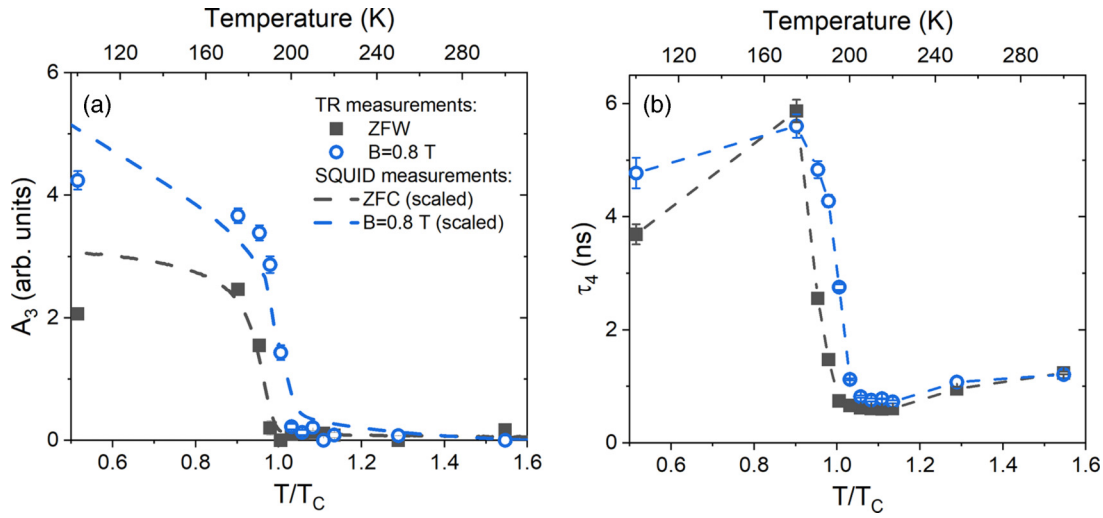

FIG. 2. (a) The fitted amplitude A_3 for zero field (black, solid squares) and an applied field of $B = 0.8$ T (blue, open circles). The dashed lines represent the related SQUID measurements, which are individually y-scaled to match the height of the curves to the time-resolved data. (b) The time constant τ_4 plotted as a function of normalized temperature (zero field—black, solid squares; 0.8 T—blue, open circles). The color-matched dashed lines are a guide to the eye. Error bars are calculated from the fit.

exponentials are necessary to describe the increase in reflectivity ($A_{1,2,3} \geqslant 0$). The fourth exponential with amplitude $A_4 < 0$ accounts for the decrease in reflectivity at the largest timescale with the time constant τ_4. Fitting results regarding the amplitude of the growth of (C) and the exponential decay time of (D) reveal a strong dependence on the phase state of LPCMO as shown in Figs. 2 and 3. For $T \gg T_C$ the reflectivity signal on the longest timescale decreases with a time constant of $\tau_4 \sim 1$ ns [see Fig. 2(b)]. When approaching the phase transition from above, τ_4 decreases first and shows a shallow minimum around 210 K, and then abruptly increases at the PT, reaching a large value of 6 ns. Attention has to be paid to the analysis of the third exponential $A_3 \exp(-\frac{t}{\tau_3})$, as for $T \gtrsim T_C$ the amplitude A_3 quickly vanishes and τ_3 (see SM [30]) is not defined anymore. Therefore, the amplitude A_3 is depicted in Figs. 2(a) and 3(a) as an indicator for the existence of this process. The vanishing of the third exponential (C) in the PMI phase clearly points towards a magnetic origin of the underlying τ_3 process. Both A_3 and τ_4 [process (D)] show a sudden increase at T_C for $B = 0$, which shifts by about 10 K in an applied field of 0.8 T, supporting the hypothesis of a magnetic origin of these processes (see Fig. 2).

Further insight into τ_3 and τ_4 can be obtained from magnetic-field-dependent measurements recorded at $T_1 = 195$ K $\approx T_C$ and at $T_2 = 200$ K. Applying Eq. (1) as before, the most significant changes are again found in A_3 and τ_4 (see Fig. 3). In particular, Fig. 3(a) shows that at a temperature of 195 K $\approx T_C$ an applied magnetic field of $B \approx 0.5$ T is of sufficient strength to lead to the appearance of process (C). In contrast, at a higher temperature of 200 K $> T_C$ this process remains absent within the range of applied fields of $B = 0$–0.8 T. In addition, we find that τ_4 can be tuned continuously by the applied magnetic field [see Fig. 3(b)]. However, as should be expected, the field sensitivity of the τ_4 process is getting weaker further away from the PT.

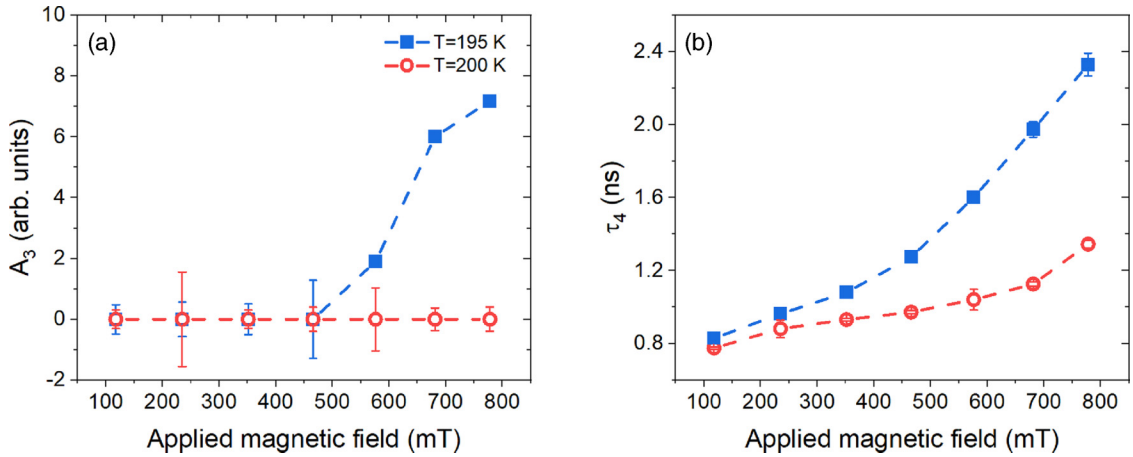

FIG. 3. Magnetic field dependence of (a) the amplitude A_3 and (b) the relaxation time τ_4 in LPCMO at $T_1 = 195$ K and $T_2 = 200$ K. Color-matched dashed lines are a guide to the eye. Error bars are calculated from the fit.

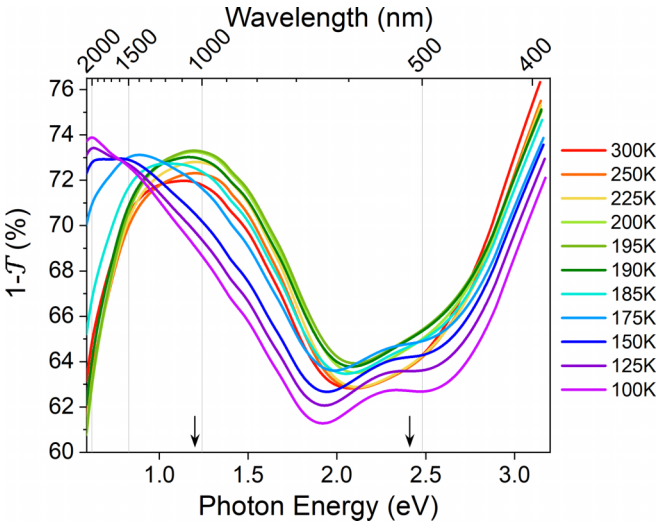

FIG. 4. Static $1-\mathcal{T}$ spectra of the LPCMO film measured in a temperature range of $T = 100$–300 K. The arrows mark the energies of the pump (1.2 eV) and the probe (2.4 eV) pulses used in the time-resolved measurements.

B. Static optical characterization

Temperature-dependent, static optical absorption data have been measured to compare the static and the dynamic optical properties as well as to use them as material parameters for FDTD simulations of the system dynamics (see below and SM [30]).

The spectra in Fig. 4 demonstrate pronounced wavelength and temperature dependencies of the optical properties, displaying a broad maximum at a photon energy of $E \sim 1.2$ eV, followed by a broad minimum at $E \sim 2.2$ eV for high temperatures, $T > T_C$, and an absorption edge for $E > 2.7$–3 eV. The spectra are in general agreement with the UV-visible data reported for optimally doped LCMO [24]. The spectral features partly originate from optical transitions between the hybridized O($2p$)-Mn states to the Mn($3d$) states. For instance, the NIR peak at $E \sim 1.2$ eV can be related to an e_g-e_g intersite transition between Mn^{3+} and Mn^{4+} bands with parallel t_{2g} core spins, the energy of which decreases when the magnetic order increases [28]. Even though out of the measurement range, $E > 3.2$ eV, the charge transfer transitions such as those from O($2p$) to Mn(e_g) bands are anticipated in the UV-visible range and in our case manifest themselves via the edge around 2.7–3.2 eV similar to the spectra of PCMO [35].

Cooling down below the MI transition temperature is accompanied by a spectral weight transfer (SWT) to lower photon energies, $E < 0.7$ eV. This SWT is most pronounced in the NIR spectral range, where the maximum at 1.2 eV at room temperature red-shifts to about 0.7 eV at 100 K. In contrast, the absorption edge for $E > 3$ eV undergoes a blue shift with decreasing temperature. The curves in Fig. 4 for $T < T_{\mathrm{MI}}$ cross in an isosbestic point at 0.8–0.9 eV, and, simultaneously, a new, shallow peak emerges at $E \sim 2.25$ eV. This peak is assumed to result from the exchange energy splitting of spin-polarized bands in the FMM state, which in the case of the measured LPCMO sample can be estimated to be ∼1.0–1.5 eV and gives rise to another possible final state for the UV-visible transitions.

The observed SWT in LPCMO, being qualitatively similar to that discussed for LCMO and other manganites [36–38], is intimately related to the coupled metal-insulator/magnetic phase transition [24,36–39]. One has to point out, that the static SWT certainly starts to develop at $T \approx T_C$, but a considerable SWT change occurs in the FMM state at $T \leqslant 175$ K, likely indicating a "pinning" of the band at $E \sim 1.2$ eV by correlated JT polarons for $175\ \mathrm{K} \leqslant T < T_C$. Note that the concentration of polarons displays a sharp maximum around T_C and is getting suppressed for $T < T_C$ in the FMM state [14,25]. It is the SWT that makes dynamic reflectivity measurements sensitive to the magnetic state of the sample [24], as evident from the data in Fig. 1.

IV. DISCUSSION

As already pointed out, the significant qualitative changes in the TR observed at the PT indicate a change of the internal relaxation pathways. Following Refs. [39,40], we identify the process related to τ_3 with spin-lattice relaxation. The appearance of this strong magnetic contribution in the TR data is a consequence of a dynamic spectral weight transfer (DSWT), analogous to the static SWT observed in the static optical characterization of LPCMO (see Fig. 4 and Ref. [39]). Within the FM phase, the excess energy flows from the lattice into the spin system after the optical excitation and the fast electron-phonon scattering. This gives rise to a demagnetization causing the DSWT, which manifests itself as an increase of $\Delta\mathcal{R}$ at $\lambda_{\mathrm{probe}} = 515$ nm (see also Ref. [28], where the static optical conductivity is maximized in the demagnetized state of LPCMO with $M = 0$). With respect to DSWT, the presence of A_3 is an indicator of the FM phase and the sensitivity of the phase state close to the PT to external magnetic fields [see Figs. 2(a) and 3(a)]. Note an important difference between the static and the dynamic SWT. Namely, the static SWT, presumably being "pinned" by correlated JT polarons, develops most strongly at $T \approx 175$ K within the FMM state, but the DSWT proceeds already at T_C with a much stronger change than in the static case. This indicates that the correlated JT polarons are destroyed by the photoexcitation of Mn^{3+} e_g states at $E \sim 1.2$ eV for times $t < 1$ ps, as discussed in the literature [20,41,42]. This process allows for the DSWT onset at the timescale $\tau_3 \sim 50$–100 ps close to T_C.

The data in Fig. 2(b) further show that the back relaxation of $\Delta\mathcal{R}(t)$ described by the time constant τ_4 drastically slows down while crossing into the FMM state from the PMI phase. This is also evidenced by the field-induced increase of $\tau_4(B)$ shown in Fig. 3(b) for $T_1 = 195$ K and $T_2 = 200$ K. External magnetic fields thereby allow one to control τ_4 close to the PT and, particularly, for $T_1 = 195$ K a moderate field of $B \sim 0.8$ T leads to an increase of τ_4 by a factor of 3.

Long-lived transients in the FM phase have been noted in earlier pump-probe studies of the related optimally doped LCMO; however, no detailed information on the variation of the relaxation time back to the initial state (here denoted τ_4) with temperature and magnetic field close to the PT was provided. Ren *et al.* [22,23] attributed the increase of the relaxation time entering the FM phase to the slow relaxation

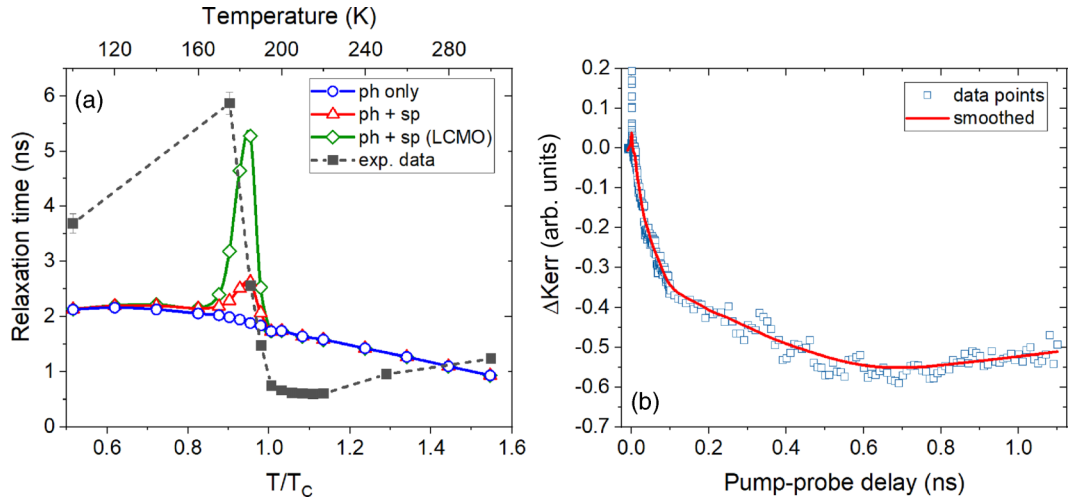

FIG. 5. (a) Comparison of relaxation times from FDTD simulations and the zero-field experiment. The blue solid line and open circles correspond to the simulation results for plain thermal transport contribution (ph only); red triangles—phonon and spin contribution (ph + sp) using the spin-specific heat of bulk LPCMO; and green diamonds—phonon and spin contribution (ph + sp) using the spin-specific heat of bulk LCMO. The dashed black line and solid squares correspond to the results from the zero-field experiment from Fig. 2(b). (b) Transient change of Kerr rotation signal at $T = 175$ K and low field of $B \approx 0.12$ T. All lines are a guide to the eye.

of localized (intragap) states via spin-lattice coupling, which exist within the temperature- and magnetic-field-dependent pseudogap in the magnetically ordered phase. Bielecki *et al.* [43] explained the long-term relaxation in LCMO by heat diffusion. Wang *et al.* [44] attributed the slow recovery of reflectivity in LCMO to long magnon lifetimes, but without giving further details. Yousefi Sarraf *et al.* [45] even discuss radiative recombination processes in the case of $La_{0.7}Sr_{0.3}MnO_3$ films.

In the case of LPCMO films, we rule out changes of thermal conductivity κ and thereby heat diffusion effects [43] as the main reason for the observed variation of τ_4 with temperature. If the experimentally observed increase in τ_4 would be due to thermal conduction, this would require a sudden change in thermal conductivity with $\kappa < 1\ \mathrm{Wm^{-1}\,K^{-1}}$ close to the PT in the FM phase, which is not observed in measurements of thermal transport of such films (see SM [30]) and also is not expected from general considerations of the evolution of thermal transport across a PM-FM metal insulator transition (MIT) in manganites [46,47]. To further verify that the observed drastic increase of the relaxation time while entering the FMM phase does not have a purely thermal origin, we performed FDTD simulations [48,49] using a modified three-temperature model (3TM) [50], which additionally considers classical thermal diffusion along the surface normal. Very briefly, the model solves a one-dimensional three-temperature model using three coupled temperature-diffusion equations for the electronic, lattice, and spin systems, taking into account the laser excitation; the different specific heats and coupling constants for electrons, phonons, and spins; and the thermal conductivity (for details see the SM [30]). We perform the simulations for two different spin-specific heats $C_S(T)$, the relevance of which will become clear in the following. We use the measured LPCMO thin film $\kappa(T)$ as given in the SM [30] and consider: (i) C_S values from bulk LPCMO data [51,52] and (ii) C_S with a peak value from bulk LCMO data [53] (see also SM [30]). These two simulations are compared by extracting the energy relaxation time τ_4 in two ways: (a) considering a contribution to the simulated $\Delta\mathcal{R}(t)$ from the phononic system only, i.e., plain thermal transport, and (b) by additionally considering a contribution of the spin system to the simulated $\Delta\mathcal{R}(t)$. Note that, even for the plain phononic signal contribution to the $\Delta\mathcal{R}(t)$ extracted from the simulation, the full 3TM is solved numerically; i.e., the energy transfer between phonons and spins is fully modeled and thereby C_S influences $\Delta\mathcal{R}(t)$. Further information on the simulation parameters can be found in the SM [30].

The $\tau_4(T)$ results, extracted from the simulated reflectivity transients, are given in Fig. 5(a) together with the experimental data for $B = 0$ (black dashed line and solid squares). The extracted temperature dependence of $\tau_4(T)$ for the plain thermal transport is given as the blue solid line and open circles (ph only). Evidently, only small and monotoneous changes occur in the timescale of thermal transport in the PMI and FMM phases in the simulation. We conclude that the phonon-mediated diffusive thermal transport as discussed in Ref. [46] for different manganites adequately describes $\Delta\mathcal{R}(t)$ of LPCMO only in the high-T PMI phase. The transition into the FMM phase, however, cannot be reproduced by plain phonon heat diffusion in the simulation. The experimentally observed increase of the relaxation time by about an order of magnitude near T_C thereby signals additional contributions to the measured $\Delta\mathcal{R}(t)$ by other, long-living excitations in the FM phase, which are imprinted onto the transient reflectivity signal. At intermediate timescales of ~100 ps, the sample demagnetization due to spin-lattice relaxation, i.e., τ_3 is already known to contribute to $\Delta\mathcal{R}(t)$ due to DSWT [24,39]. In turn, $\tau_4(T)$ within the FMM phase can be expected to be significantly influenced by the remagnetization back to the equilibrium FMM state due to DWST with opposite direction and thus opposite sign in $\Delta\mathcal{R}(t)$. The red solid line and open triangles (ph + sp) in Fig. 5(a) show the effects of additionally considering a spin contribution to $\Delta\mathcal{R}(t)$ using values for the spin-specific heat for bulk LPCMO from

[51,52]. The τ_4 extracted from the simulations shows a rise at the PT, which is directly connected to the increased spin-specific heat and thereby the additional energy transfer from the lattice to the spin system. While this increase already highlights the additional energy dissipation channel, the effect is smaller than that observed in the experiment. In comparison, the green solid line and open diamonds (ph + sp LCMO) in Fig. 5(a) show the resultant $\tau_4(T)$ for using the larger peak value of C_S of the closely related CMR material LCMO from Ref. [53]. The increase in the relaxation time is now of the right order of magnitude, even though the experimental value at low T is underestimated. Keeping in mind that in both cases the spin-specific heat values are for bulk samples and not for thin films, the simulation results strongly indicate that the increase in relaxation time observed in the experiment is given by the divergence of the spin-specific heat of the system at the FM PT and the resulting slow magnetization dynamics. Thereby, considering the approximations made, the connection of the spin-specific heat with the measured increase of relaxation time appears to be well established. Note that the shallow minimum in the experimental $\tau_4(T)$ around 210 K is not reproduced by the simulation using the statically measured $\kappa(T)$, possibly indicating an additional transient energy loss channel in the polaronic intermediate phase.

To corroborate that the increase in τ_4 below T_C is indeed related to the spin dynamics of the film, we carried out time-resolved magneto-optical Kerr measurements of the magnetization dynamics slightly below T_C [see Fig. 5(b)]. The data clearly reveal de- and remagnetization on sub-nanosecond ($\sim\tau_3$) and nanosecond ($\sim\tau_4$) timescales, respectively. This result underlines that the observed reflectivity signal in the FM phase can be understood as superimposed responses of the electrons and the lattice, as well as the spin system. In contrast to the PM state, where the main energy dissipation path is defined by the thermal conductivity, a part of the absorbed energy in the ferromagnetic phase is stored temporarily in the disorder of the spin system. Thus, the relaxation back to the ground state, τ_4, which encompasses both the thermal transport and the reorientation of the spins, increases by the contribution of the spin relaxation, which exhibits critical slowing down while approaching T_C [54,55]. Thereby, the increase of τ_4 appearing in the FM state reflects mainly the spin dynamics of the system, as thermal transport by phonons occurs on the ∼2-ns timescale within the FM phase as shown by the FDTD simulations [black line and data in Fig. 5(a)].

In summary, the main difference between the insulating states, where no macroscopic magnetization exists, and the macroscopically spin-ordered FM state is that in the FM phase laser-induced demagnetization occurs and the macroscopic recovery of the ordered spin state takes significantly longer than the simultaneously occurring thermal diffusion out of the excited sample region. The timescale of the recovery of spin order is imprinted onto the reflectivity signal by DSWT.

While this line of reasoning is consistent with the general observations made experimentally, it is worth pointing out an interesting discrepancy. For a system showing a first-order PT, no large changes in specific heat are generally expected, and indeed the spin-specific heat of bulk LPCMO is small [51,52]. As indicated by the comparison of simulations and experimental data, the thin film, however, possibly exhibits a relatively large and broad change in C_S at the PT (similar as indirectly stated for LCMO thin films in Ref. [39]). One possible explanation is that in our experiments, the transition tends to be more like a second-order PT and less like a first-order PT compared to static measurements of bulk LPCMO. Two possible interpretations come to mind: First, thin LPCMO film samples are generally more ordered (or less phase separated) close to the PT than bulk samples, or, second, the laser excitation quasi-instantaneously destroys the correlation of the JT polarons [20,41,42], weakening or removing the disorder/phase separation and leading to a PT more akin to second order as in LCMO, where only a tiny amount of correlated polarons exists [14]. The second interpretation could potentially also explain the shallow minimum in the experimental $\tau_4(T)$ around 210 K, as liberating the electrons from the correlated JT polarons would give rise to an additional electronic contribution to thermal transport in that temperature range not captured in the FDTD simulation using the quasistatic $\kappa(T)$. We aim to investigate these questions in the future by excitation- and fluence-dependent studies.

Coming back to the different explanations given in the literature [22,23,43–45], our experimental observations and modeling allow us to clearly rule out changes in thermal transport in explaining the observed changes in the recovery of the ground state. On the other hand, a connection to the spin dynamics is clearly established, as also for Refs. [22,23,44]. However, in contrast to the model of Ren *et al.* [22,23], which has to assume the existence of long-living states and specific changes in the band structure, the only relevant input parameter in our model is the spin-specific heat, which is taken from measurements on related samples. A radiative decay mechanism similar to semiconductors, as mentioned by Yousefi Sarraf *et al.* [45], seems generally unlikely, as it is unclear why such an effect should become dominant entering a metallic state from an insulating, gapped one. Also, radiative recombination is a process dominant in intrinsic semiconductors, whereas the studied systems are all to be considered hole-doped. In general, we expect our description to be valid not only for LPCMO but also for LSMO and LCMO, as well as further manganites with a FM to PM phase transition.

The high sensitivity of τ_4 to moderate external magnetic fields [see Fig. 3(b)] stems from the suppression of magnetic disorder, which occurs due to the field-induced melting of the AFM coupling, which is mediated by correlated polarons in LPCMO [14]. This effect shifts the onset of the τ_4 increase to the field-induced higher T_C and is the main signature of the influence of polaronic quasiparticles on nanosecond nonequilibrium dynamics. Note, even though correlated polarons are mediating the MIT in LPCMO, the observed increase in τ_4 at the PT is in our understanding due to spin ordering and not due to the appearance of a correlated polaronic phase. Our data do not allow us to draw conclusions about the lifetime or recovery time of such correlated polarons in LPCMO, which are possibly modified during the laser excitation, as mentioned before. Rather, the change in the relaxation back to the initial state [process (D) in Fig. 1] in amplitude and duration with magnetic field close to the PT reflects the amount of energy that can be transferred and stored in spin excitations.

V. SUMMARY

The temperature- and magnetic-field-dependent energy relaxation after femtosecond optical excitation was studied across the phase transition in colossal magnetoresistive $(La_{0.6}Pr_{0.4})_{0.7}Ca_{0.3}MnO_3$ thin films. We observed large and small relaxation times within the ferromagnetic metallic phase and the paramagnetic insulating phase, respectively. Comparing experimental data with finite-difference time-domain simulations, the energy dissipation in the PMI phase was shown to be dominated by thermal transport. In contrast, a strong increase in the relaxation time within the FMM phase is caused by the critical slowing down of spin dynamics close to the PT due to the increase of the spin-specific heat, while thermal transport remains largely unchanged. The spin system contributes to the transient reflectivity signal via a dynamical spectral weight transfer, which is connected to the magnetization dynamics. Correlated polarons, even though crucially important for the equilibrium properties of the system in the phase transition region, do, rather surprisingly, not directly influence the observed energy relaxation dynamics. Still, our results show that the ground-state nanoscale phase separation close to the phase transition with FM domains, AFM coupled by correlated JT polarons, leads to a strong sensitivity of the system to magnetic fields and allows one to continuously tune the electronic state of the system by reorienting the FM domains. The correlated JT polarons as mediators of the phase separation thus enable one to control the spin and electron dynamics by a moderate magnetic field $B < 1$ T, making LPCMO an attractive model system for advanced control of energy harvesting and/or information processing.

ACKNOWLEDGMENTS

We thank S. Merten for the design of the static optical setup. C.S., T.T., V.B.-B., V.M., H.U., and D.S. acknowledge the Deutsche Forschungsgemeinschaft (DFG) for funding within projects A02 and A06 of the CRC 1073 (Project No. 217133147). K.S. and S.M. acknowledge the DFG for funding through DFG Project No. 399572199.

[1] H. Y. Hwang, S.-W. Cheong, P. G. Radaelli, M. Marezio, and B. Batlogg, Phys. Rev. Lett. **75**, 914 (1995).
[2] Y. Tokura, Rep. Prog. Phys. **69**, 797 (2006).
[3] V. Moshnyaga and K. Samwer, Ann. Phys. **523**, 652 (2011).
[4] S. Jin, T. H. Tiefel, M. McCormack, R. A. Fastnacht, R. Ramesh, and L. H. Chen, Science **264**, 413 (1994).
[5] S. Jin, M. McCormack, T. H. Tiefel, and R. Ramesh, J. Appl. Phys. **76**, 6929 (1994).
[6] R. von Helmolt, J. Wecker, B. Holzapfel, L. Schultz, and K. Samwer, Phys. Rev. Lett. **71**, 2331 (1993).
[7] Y. Tokura and Y. Tomioka, J. Magn. Magn. Mater. **200**, 1 (1999).
[8] M. Uehara, S. Mori, C. H. Chen, and S.-W. Cheong, Nature (London) **399**, 560 (1999).
[9] C. Şen, G. Alvarez, and E. Dagotto, Phys. Rev. Lett. **98**, 127202 (2007).
[10] J. Burgy, M. Mayr, V. Martin-Mayor, A. Moreo, and E. Dagotto, Phys. Rev. Lett. **87**, 277202 (2001).
[11] C. Zener, Phys. Rev. **81**, 440 (1951).
[12] P. W. Anderson and H. Hasegawa, Phys. Rev. **100**, 675 (1955).
[13] P.-G. de Gennes, Phys. Rev. **118**, 141 (1960).
[14] V. Moshnyaga, A. Belenchuk, S. Hühn, C. Kalkert, M. Jungbauer, O. I. Lebedev, S. Merten, K.-Y. Choi, P. Lemmens, B. Damaschke, and K. Samwer, Phys. Rev. B **89**, 024420 (2014).
[15] C. P. Adams, J. W. Lynn, Y. M. Mukovskii, A. A. Arsenov, and D. A. Shulyatev, Phys. Rev. Lett. **85**, 3954 (2000).
[16] P. Dai, J. A. Fernandez-Baca, N. Wakabayashi, E. W. Plummer, Y. Tomioka, and Y. Tokura, Phys. Rev. Lett. **85**, 2553 (2000).
[17] T. Y. Koo, V. Kiryukhin, P. A. Sharma, J. P. Hill, and S.-W. Cheong, Phys. Rev. B **64**, 220405(R) (2001).
[18] V. Kiryukhin, T. Y. Koo, H. Ishibashi, J. P. Hill, and S.-W. Cheong, Phys. Rev. B **67**, 064421 (2003).
[19] S. Merten, O. Shapoval, B. Damaschke, K. Samwer, and V. Moshnyaga, Sci. Rep. **9**, 2387 (2019).
[20] A. Caviezel, U. Staub, S. L. Johnson, S. O. Mariager, E. Möhr-Vorobeva, G. Ingold, C. J. Milne, M. Garganourakis, V. Scagnoli, S. W. Huang, Q. X. Jia, S.-W. Cheong, and P. Beaud, Phys. Rev. B **86**, 174105 (2012).
[21] K.-J. Jang, J. Lim, J. Ahn, J.-H. Kim, K.-J. Yee, and J. S. Ahn, Phys. Rev. B **81**, 214416 (2010).
[22] Y. H. Ren, H. B. Zhao, G. Lüpke, C. S. Hong, N. H. Hur, Y. F. Hu, and Q. Li, J. Chem. Phys. **121**, 436 (2004).
[23] Y. H. Ren, M. Ebrahim, H. B. Zhao, G. Lüpke, Z. A. Xu, V. Adyam, and Q. Li, Phys. Rev. B **78**, 014408 (2008).
[24] A. I. Lobad, A. J. Taylor, C. Kwon, S. A. Trugman, and T. R. Gosnell, Chem. Phys. **251**, 227 (2000).
[25] M. Michelmann, V. Moshnyaga, and K. Samwer, Phys. Rev. B **85**, 014424 (2012).
[26] S. Hühn, M. Jungbauer, M. Michelmann, F. Massel, F. Koeth, C. Ballani, and V. Moshnyaga, J. Appl. Phys. **113**, 17D701 (2013).
[27] V. Moshnyaga, L. Sudheendra, O. I. Lebedev, S. A. Köster, K. Gehrke, O. Shapoval, A. Belenchuk, B. Damaschke, G. van Tendeloo, and K. Samwer, Phys. Rev. Lett. **97**, 107205 (2006).
[28] M. Jungbauer, S. Hühn, J.-O. Krisponeit, and V. Moshnyaga, New J. Phys. **16**, 063034 (2014).
[29] V. Moshnyaga, I. Khoroshun, A. Sidorenko, P. Petrenko, A. Weidinger, M. Zeitler, B. Rauschenbach, R. Tidecks, and K. Samwer, Appl. Phys. Lett. **74**, 2842 (1999).
[30] See Supplemental Material at http://link.aps.org/supplemental/10.1103/PhysRevB.107.085115 for further sample characterization, information on the transient reflectivity setup, details on static optical measurements, further data evaluation as well as details on the finite-difference time-domain model, and data on thermal conductivity. Further references therein, here listed as Refs. [56–68] contain additional information concerning experimental measurement procedures, data evaluation, and material parameters discussed in the Supplemental Information.
[31] A. S. Hassanien and A. A. Akl, Superlattices Microstruct. **89**, 153 (2016).

[32] J. I. Pankove, *Optical Processes in Semiconductors* (Dover Publications, New York, 1975).
[33] S. Y. El-Zaiat, Optik **124**, 157 (2013).
[34] E. Nichelatti, J. Opt. A: Pure Appl. Opt. **4**, 400 (2002).
[35] S. Mildner, J. Hoffmann, P. E. Blöchl, S. Techert, and C. Jooss, Phys. Rev. B **92**, 035145 (2015).
[36] K. H. Kim, J. H. Jung, and T. W. Noh, Phys. Rev. Lett. **81**, 1517 (1998).
[37] Y. Okimoto, T. Katsufuji, T. Ishikawa, A. Urushibara, T. Arima, and Y. Tokura, Phys. Rev. Lett. **75**, 109 (1995).
[38] S. G. Kaplan, M. Quijada, H. D. Drew, D. B. Tanner, G. C. Xiong, R. Ramesh, C. Kwon, and T. Venkatesan, Phys. Rev. Lett. **77**, 2081 (1996).
[39] A. I. Lobad, R. D. Averitt, C. Kwon, and A. J. Taylor, Appl. Phys. Lett. **77**, 4025 (2000).
[40] A. I. Lobad, R. D. Averitt, and A. J. Taylor, Phys. Rev. B **63**, 060410(R) (2001).
[41] M. Fiebig, K. Miyano, Y. Tomioka, and Y. Tokura, Appl. Phys. B **71**, 211 (2000).
[42] V. Esposito, M. Fechner, R. Mankowsky, H. Lemke, M. Chollet, J. M. Glownia, M. Nakamura, M. Kawasaki, Y. Tokura, U. Staub, P. Beaud, and M. Först, Phys. Rev. Lett. **118**, 247601 (2017).
[43] J. Bielecki, R. Rauer, E. Zanghellini, R. Gunnarsson, K. Dörr, and L. Börjesson, Phys. Rev. B **81**, 064434 (2010).
[44] H. Wang, Z. Jin, X. Liu, Z. Zhang, X. Lin, Z. Cheng, and G. Ma, Appl. Phys. Lett. **110**, 252407 (2017).
[45] S. Yousefi Sarraf, S. Singh, A. C. Garcia-Castro, R. Trappen, N. Mottaghi, G. B. Cabrera, C.-Y. Huang, S. Kumari, G. Bhandari, A. D. Bristow, A. H. Romero, and M. B. Holcomb, ACS Nano **13**, 3457 (2019).
[46] J. L. Cohn, J. J. Neumeier, C. P. Popoviciu, K. J. McClellan, and T. Leventouri, Phys. Rev. B **56**, R8495 (1997).
[47] D. W. Visser, A. P. Ramirez, and M. A. Subramanian, Phys. Rev. Lett. **78**, 3947 (1997).
[48] B. Kressdorf, T. Meyer, M. ten Brink, C. Seick, S. Melles, N. Ottinger, T. Titze, H. Meer, A. Weisser, J. Hoffmann, S. Mathias, H. Ulrichs, D. Steil, M. Seibt, P. E. Blöchl, and C. Jooss, Phys. Rev. B **103**, 235122 (2021).
[49] H. Ulrichs, D. Meyer, M. Müller, M. Mansurova, and F. Döring, AIP Conf. Proc. **1763**, 040004 (2016).
[50] E. Beaurepaire, J.-C. Merle, A. Daunois, and J.-Y. Bigot, Phys. Rev. Lett. **76**, 4250 (1996).
[51] M. Quintero, J. Sacanell, L. Ghivelder, A. M. Gomes, A. G. Leyva, and F. Parisi, Appl. Phys. Lett. **97**, 121916 (2010).
[52] M. Michelmann, Temperatur- und Magnetfeldabhängigkeit der elastischen Konstanten eines (La,Pr,Ca)-Manganats, Masters thesis, Georg-August-Universität, Göttingen, 2010.
[53] N. Kumar, H. Kishan, A. Rao, and V. P. S. Awana, J. Appl. Phys. **107**, 083905 (2010).
[54] U. Atxitia, O. Chubykalo-Fesenko, J. Walowski, A. Mann, and M. Münzenberg, Phys. Rev. B **81**, 174401 (2010).
[55] N. Kazantseva, U. Nowak, R. W. Chantrell, J. Hohlfeld, and A. Rebei, Europhys. Lett. **81**, 27004 (2008).
[56] W. Li, B. He, C. Zhang, S. Liu, X. Liu, S. Middey, J. Chakhalian, X. Wang, and M. Xiao, Appl. Phys. Lett. **108**, 132601 (2016).
[57] J. S. Browder and S. S. Ballard, Appl. Opt. **8**, 793 (1969).
[58] V. Moshnyaga and K. Samwer, Crystals **9**, 489 (2019).
[59] M. Kazan, G. Guisbiers, S. Pereira, M. R. Correia, P. Masri, A. Bruyant, S. Volz, and P. Royer, J. Appl. Phys. **107**, 083503 (2010).
[60] R. I. Hickson, S. I. Barry, G. N. Mercer, and H. S. Sidhu, Math. Comput. Modell. **54**, 210 (2011).
[61] G. M. Müller, J. Walowski, M. Djordjevic, G.-X. Miao, A. Gupta, A. V. Ramos, K. Gehrke, V. Moshnyaga, K. Samwer, J. Schmalhorst, A. Thomas, A. Hütten, G. Reiss, J. S. Moodera, and M. Münzenberg, Nat. Mater. **8**, 56 (2009).
[62] O. Deparis, Opt. Lett. **36**, 3960 (2011).
[63] P. G. Radaelli, G. Iannone, M. Marezio, H. Y. Hwang, S.-W. Cheong, J. D. Jorgensen, and D. N. Argyriou, Phys. Rev. B **56**, 8265 (1997).
[64] C. Thomsen, J. Strait, Z. Vardeny, H. J. Maris, J. Tauc, and J. J. Hauser, Phys. Rev. Lett. **53**, 989 (1984).
[65] R. D. Averitt, A. I. Lobad, C. Kwon, S. A. Trugman, V. K. Thorsmølle, and A. J. Taylor, Phys. Rev. Lett. **87**, 017401 (2001).
[66] D. G. Cahill, Rev. Sci. Instrum. **61**, 802 (1990).
[67] T. Borca-Tasciuc, A. R. Kumar, and G. Chen, Rev. Sci. Instrum. **72**, 2139 (2001).
[68] S. Miyoshi, A. Kaimai, H. Matsumoto, K. Yashiro, Y. Nigara, T. Kawada, and J. Mizusaki, Solid State Ionics **175**, 383 (2004).